Ocean Modelling 90 (2015) 16–28

Contents lists available at ScienceDirect

Ocean Modelling

journal homepage: www.elsevier.com/locate/ocemod

Virtual Special Issue
Gulf of Mexico Modelling - Lessons from the spill

Numerical simulations of turbulent thermal, bubble and hybrid plumes

Alexandre Fabregat[a,*], William K. Dewar[c], Tamay M. Özgökmen[b], Andrew C. Poje[a], Nicolas Wienders[c]

[a] Department of Mathematics, City University of New York, College of Staten Island, 2800 Victory Boulevard, Staten Island, New York, NY 10314, United States
[b] Rosenstiel School of Marine and Atmospheric Science, University of Miami, 4600 Rickenbacker Causeway, Miami, FL 33149-1098, United States
[c] Earth, Ocean and Atmospheric Science, Florida State University, P.O. Box 3064520, Tallahassee, FL 32306-4520, United States

ARTICLE INFO

Article history:
Received 10 September 2014
Revised 16 January 2015
Accepted 25 March 2015
Available online 9 April 2015

Keywords:
Multiphase flows
Buoyant plumes
Deepwater blowouts

ABSTRACT

To understand the near-field dynamics of blowout plumes such as the one produced by the 2010 Deepwater Horizon oil spill in the Gulf of Mexico, the effects of gas bubbles on turbulent mixing and entrainment are studied via turbulence resolving simulations. We compare the evolution of three plumes where extremely large buoyancy anomalies are produced either thermally (single phase), solely by an imposed gas phase volume fraction, or by a combination of both buoyancy forcings. The plumes, with identical volume, momentum and buoyancy fluxes at the inlet, are released into an environment stratified with a constant temperature gradient. To clarify the first-order effects of dynamically active, dispersed bubbles, we employ a simple model which neglects the momentum of the gas phase while retaining bubble induced buoyancy in the seawater momentum equation. The gas phase is then distinguished by a single, measurable parameter, the slip velocity relative to that of the liquid phase. We find that bubbles, parameterized simply by a constant slip velocity, without any explicit assumptions of direct bubble induced turbulent production, significantly increase turbulent mixing in the plume in agreement with previous experimental results. Examination of mean momenta and turbulent kinetic energy budgets shows that the increased turbulence is due to direct modification of the mean profiles of both the momentum and the active scalar fields by the slipping gas phase. The narrowing of the active scalar field in the two-phase flow results in larger direct buoyancy production of turbulent energy at all vertical levels. The turbulence production is, however, primarily mechanical. At modest values of z/D, where the slip velocity is only a small fraction of the liquid phase velocity, slip stretches the mean vertical velocity field producing larger radial gradients and increased conversion of mean to turbulent energy. This first order effect, acting on the mean vertical velocity component and not directly on the turbulence, implies that even relatively small gas volume fractions significantly enhance turbulent mixing with respect to a single phase plume.

1. Introduction

This work, motivated by the 2010 Deepwater Horizon (DwH) incident in the northern Gulf of Mexico, focuses on modeling and simulating the near-field region of flows driven by the extreme buoyancy fluxes typical of deep water oil well blowouts (Camilli et al., 2010). Deepwater blowout plumes are formed by the sustained point release of a hot, multiphase wellhead mixture through the riser pipe. The resulting buoyancy flux, released into a stratified fluid, was thermally equivalent to $B_0 = \mathcal{O}(1\,\mathrm{GW})$ in the Deepwater Horizon case (McNutt et al., 2011). The magnitude of the buoyancy anomaly, sustained over a period of months, and the extremely large range of spatial scales involved (0.5 m source at 1500 m depth) implies that these multiphase plumes are far from realizable laboratory conditions (Lima Neto, 2012). The extremely large, sustained buoyancy fluxes also imply that the wellhead convection problem has the potential to dynamically alter the larger scale, rotating and stratified environment.

The DwH release underscored the need for rapid and informed response to such events. An integral part of that response is the prediction of both the distribution of hydrocarbon effluent throughout the water column and the eventual form of its expression at the ocean

* Corresponding author. Tel.: +1 7189823617.
E-mail address: fabregat.alex@gmail.com, Alex.Fabregat@csi.cuny.edu (A. Fabregat).

http://dx.doi.org/10.1016/j.ocemod.2015.03.007
1463-5003/

surface. Since the near-field turbulent entrainment plays a critical role in the evolution of the plume buoyancy, mass and momentum fluxes, understanding and modelling *multiphase* plume dynamics in the vicinity of the release is potentially critical to accurate prediction of the near-surface pollution transport problem over of the *last mile*, where the spill encounters the public. The inlet buoyancy flux generates a strongly turbulent buoyant plume in which sea water entrained from the environment is mixed with the plume core fluids as they move along the water column. The evolution of the plume is strongly affected by the level of turbulent mixing and entrainment in the near-field with the 'entrainment coefficient' being the main parameter in classic integral solution approaches (Morton et al., 1956). It is well-known that the presence of a gas phase changes the turbulent transport properties, with bubble plumes typically exhibiting larger turbulence levels (McDougall, 1978; Milgram, 1983). There are distinct differences in the along-column effluent distribution in single and multiphase cases (Asaeda and Imberger, 1993; Lemckert and Imberger, 1993). The effects of bubbles on turbulent dynamics are studied here by comparing plumes distinguished only by the phase distribution of the (fixed) inlet buoyancy flux, either thermal (single phase) or due to the presence of gas (multiphase).

Modeling in complete, accurate detail, the physicochemical dynamics of the high pressure release of hot, multicomponent, multiphase effluent into a stratified, turbulent ocean environment is beyond our present theoretical and computational abilities. As in the case of the DwH incident, both short and intermediate term prediction and analysis of any future event will rely on simplified models for which there is existing literature. How the validity of underlying assumptions and the values of explicit parametrizations in simplified models change when such models are scaled up from the laboratory to the environment requires careful examination of the many physical and chemical processes involved.

Given their environmental and industrial importance, buoyant plumes have been the focus of considerable study. Schmidt (1941) presented an earlier dimensional analysis of thermal plumes, and the problem has attracted the attention of Batchelor (1954), Morton et al. (1956), Turner (1973; 1969) and others. Many of these efforts represent the depth dependence bulk plume measure, like momentum and buoyancy flux, in terms of the basic system parameters. Turner discusses several laboratory experiments in support of the scaling laws. List and Imberger (1973) is an early reference on plumes in stratified environments, pointing out the creation of intrusion layers. McDougall (1978) performed perhaps the first experiments of two phase convective systems, discussing the presence of dual plumes. Classification of bubble plume experiments and observations appear in Lemckert and Imberger (1993), Socolofsky et al. (2002) and Socolofsky and Adams (2005). Classical modeling efforts directed at oil spill prediction have been posed as a Lagrangian problem, in which integral plume measures, like momentum flux and centerline trajectory were computed (Zheng and Yapa, 2003). These have been tested against laboratory and limited field experiments and have demonstrated skill. In all cases, the equations are closed by relating the turbulent radial flux to the characteristic mean vertical velocity via an entrainment coefficient (Morton et al., 1956). Enhanced turbulent mixing of vertical momentum due to multiphase physics is typically modelled by a larger momentum amplification factor, reducing the vertical momentum growth rate in comparison to single phase plumes.

The goal of the present work is to understand and quantify, in the context of turbulence resolving simulations, basic physical properties of plumes driven by the extreme values of the expected buoyancy flux in a deepwater blowout. This fills a significant gap in our present knowledge of deep spills, specifically the role played by the gas in increasing the turbulent mixing. The DwH blowout involved both oil and gas escaping from the well head (McNutt et al., 2011). As a first step, we isolate the effect of bubbles on the turbulence by considering idealized situations where admittedly important physicochemical phenomena (hydrate formation, dissolution or biodegradation) are neglected and the input buoyancy is due solely to thermal and gas contributions. Given that it is not possible in such incidents to determine the exact proportions of oil and gas involved at specific instances or periods, we explore distinctions in the turbulent behavior of plumes produced by varying the relative importance of the inlet gas buoyancy contribution. Such idealized cases are closer to the flow configuration used in most experimental studies of bubble plumes but differ significantly in the magnitude of the inlet buoyancy flux. Moreover, to our knowledge there are no experimental observations of the combined effects of thermal and gas sources. Laboratory experiments of bubble and oil plumes face a number of challenges. Usually the tank size is limited in the vertical direction and the reflection of the plume from the upper boundary can change the flow field significantly. Due to box-filling problems, limited tank size necessarily limits both the inlet oil flux and the overall time scales of experiments. To attain flows that are highly turbulent, nozzle sizes used in the laboratory are typically on the order of a few millimeters. Even then, the observation period for measurements is typically minutes (Brandvik et al., 2013; Johansen et al., 2013). It is unclear how representative plumes from such small nozzles are for the real oceanic case. Finally, we are not aware of laboratory experiments of hybrid (bubble and oil) plumes and highly-parameterized models do not allow direct exploration of the details of the turbulent behavior in such cases.

Computationally, significant efforts have been devoted to the study of multiphase plumes at oceanographic scales in the context of CO_2 sequestration (Alendal and Drange, 2001; Sato and Sato, 2002). These studies emphasize the effects of physico-chemical phenomena on overall plume behavior using standard eddy-viscosity and eddy-duffusivity models to account for turbulent transport. Characterization of the differences in the turbulent mixing between single and multiphase plumes requires explicit resolution of finer scale motions. This is particularly important for plumes where differences in near-field turbulent entrainment processes significantly influence far field behavior and, consequently, the overall distribution of effluents in the water column including the fraction of effluent reaching the ocean surface.

While complete spatial and temporal descriptions via direct numerical simulations are typically unfeasible even for laboratory scale plumes, large-eddy simulations (LES) of bubble plumes have been conducted (Buscaglia et al., 2002; Deen et al., 2001; Niceno et al., 2008) using finite-difference or finite-volume discretizations to explicitly resolve the largest, most energetic scales while parametrizing sub-grid scales by Smagorinsky models. In this work the approach is slightly different: instead of low-order spatial discretizations, we use high-order spectral element methods characterized by exponential convergence. In lieu of explicit Smagorinsky models, the specifics of which are still uncertain for bubbly flows (Dhotre et al., 2013), we adopt an alternate approach based on spectral filtering (Karamanos and Karniadakis, 2000; Koal et al., 2012). Progressive filtering of the highest modes of the Legendre polynomial approximations is equivalent to a hyperviscosity subgrid-scale model whose influence is explicitly confined to near-grid scale processes (Boyd, 1998; Fischer and Mullen, 2001). This approach has been shown to maintain spectral accuracy with increasing resolution and provide resolution independent solutions. The computational efficiency afforded permits the explicit resolution of a larger range of spatial scales.

For large-scale plumes, adequate turbulence resolution, in reasonable time, on available computational resources requires both limiting the vertical extent of the domain and simplifying the full multiphase equation set. Starting from the conservation equations for multiphase systems, following (Sokolichin et al., 2004), we derive a simplified, Boussinesq model by neglecting the momentum carried by the gas which is much smaller than that of the liquid phase. Even with

this simplification, open questions remain concerning the details of dispersed phase modelling of liquid-gas systems. Bubbles in a turbulent flow can be subjected to a wide variety of phenomena that may significantly affect the overall dynamics. Bubble breakup and coalescence, bubble oscillation and rotation and other bubble–bubble and bubble–liquid interactions have been explicitly modeled as *bubble induced* turbulence (Clift et al., 1978; Dhotre et al., 2009; Sato et al., 1981; Tomiyama, 1998). Although there are numerical studies devoted to understanding the physics behind these processes (Esmaeeli and Tryggvason, 1998; 1999; Fox, 2012; Kuwagi and Ozoe, 1999), proper parameterization and modeling remains unclear (Sokolichin et al., 2004). In a typical environmental blowout, with reasonably small gas volume fractions at the inlet, effects associated with individual bubbles are expected to be small given the levels of local shear produced by the large buoyancy flux at the inlet and the expected small bubble diameters (Lima Neto et al., 2008a). Accordingly, we argue that the most relevant parameter in the first order physics of dispersed bubbles is the slip velocity of the gas phase relative to the liquid. Here we simply set this parameter to a constant value consistent with that reported in experimental plumes (Lima Neto et al., 2008b; Simiano, 2005), numerical simulations (Dhotre et al., 2009) and estimations of the rise velocity for gas bubbles during the DwH spill (Socolofsky et al., 2011).

The current model, with relatively minor modifications, can be used for a wide range of oceanographic multiphase plume problems. In particular, and perhaps most importantly, oil phase buoyancy contributions can be explicitly divorced from the thermal field by considering a mixture model for the liquid phases. Physicochemical effects can be modeled via evolving distributions of slip velocities (Lima Neto et al., 2008b) and extensions to the study of multiple intrusions in the water column (Asaeda and Imberger, 1993; Socolofsky and Adams, 2003; 2005) and rotating systems (Helfrich, 1994; Julien et al., 1999) are possible.

2. Mathematical model

2.1. Multiphase plumes

Equations describing the evolution of a mixture of fluids, each member of which is denoted by the subscript k, are introduced. By expressing in the continuum limit the transport equations obtained using the Volume of Fluid approach, we avoid here the subtleties of working with discrete phases in deriving a set of partial differential equations (Buscaglia et al., 2002).

The mass conservation equation for phase k can be written as

$$\frac{\partial}{\partial t}\left(\alpha_k \rho_k\right) + \nabla \cdot \left(\alpha_k \rho_k \tilde{\mathbf{u}}_k\right) = 0, \tag{1}$$

where t is time and ρ_k, α_k and $\tilde{\mathbf{u}}_k = [\tilde{u}, \tilde{v}, \tilde{w}]_k$ are density, volume fraction and Cartesian velocity field for the phase k respectively. The assumption of continuous phase distributions is implicit in (1).

Similarly, the momentum equation for the phase k is

$$\frac{D}{Dt}\left(\alpha_k \rho_k \tilde{\mathbf{u}}_k\right) = -\alpha_k \nabla p + \nabla \cdot \alpha_k \boldsymbol{\tau}_k + \alpha_k \rho_k \mathbf{g} + \mathbf{M}_k, \tag{2}$$

where p is pressure, usually taken to be equal in each phase (Drew, 1983), $\nabla \cdot \alpha_k \boldsymbol{\tau}_k$ are the molecular and turbulent diffusive terms for phase k, $\mathbf{g} = -9.8\hat{\boldsymbol{k}}\,\mathrm{m\,s^{-2}}$ is the gravity acceleration vector aligned with the vertical coordinate z and $D/Dt = \partial/\partial t + \tilde{\mathbf{u}} \cdot \nabla$ stands for the material derivative. Any momentum transfer between phases is accounted in the $\mathbf{M}_k$ term and we require

$$\sum_k \mathbf{M}_k = 0, \tag{3}$$

i.e. viscous interactions within the fluid do not affect the bulk momentum.

In this work it is assumed that there are only liquid and gas phases identified as $k = l, b$ respectively. Therefore, for a two-phase plume $\alpha_l + \alpha_b = 1$ and $\mathbf{M}_l = -\mathbf{M}_b$. The bubble plume forms when the gas phase is injected as a continuous stream into the liquid phase. The bubbles rise through the liquid column faster than the liquid due to the lower density of the gas. The difference between the velocities of the two phases is known as the slip velocity $\tilde{\mathbf{u}}_s$, i.e.

$$\tilde{\mathbf{u}}_s = \tilde{\mathbf{u}}_b - \tilde{\mathbf{u}}_l. \tag{4}$$

The gas at the well head is dominantly methane which at 1200 m is approximately $\rho_b = 80\,\mathrm{kg\,m^{-3}}$, as compared to seawater at $\rho_0 = 1050\,\mathrm{kg\,m^{-3}}$. During ascent, the pressure on the bubble changes dramatically. Approximating the gas state equation by the ideal gas law results in an expansion of the bubble that may alter the value of the slip velocity (Lima Neto et al., 2008b). For much of the fluid column this is a small effect. For example, moving from 1000 m to 500 m reduces the pressure by half, resulting in a radial expansion of $2^{1/3} \approx 1.3$. At the same time, the methane will dissolve into the seawater and be consumed by microbes (Crespo-Medina et al., 2014), effects that will reduce bubble volume. Biogeochemistry effects (Yapa and Dissanayake, 2012) are not considered explicitly in this work and instead the gas slip velocity is assumed to be constant. In any case, gas density is small relative to fluid density, $\rho_b/\rho_0 \ll 1$.

In these simulations, we adopt a simple seawater equation of state

$$\rho_l = \rho_0 + \rho_l' = \rho_0\left[1 - \beta(T - T_0)\right], \tag{5}$$

where the T and ρ_l' stand respectively for temperature and liquid density fluctuation with respect to the reference state, T_0 and ρ_0, corresponding to the unperturbed seafloor conditions. $\beta = 2 \times 10^{-4}\,\mathrm{K}$ is the sea water thermal expansion coefficient. This is only for convenience; extensions to full equations of state are straightforward. It is also useful to write the temperature T as

$$T = \theta + T_0 + \Gamma(z), \tag{6}$$

where θ represents the temperature anomaly obtained after subtracting the background stratification profile $T_0 + \Gamma(z)$. In this work we assumed a linear profile $\Gamma(z) = \zeta z$ with slope $\zeta = 0.05\,\mathrm{K\,m^{-1}}$. Typical stratification slopes are $\mathcal{O}(0.01\,\mathrm{K\,m^{-1}})$ (Dehaan and Sturges, 2005). Thus, the equation of state (5) for seawater is

$$\rho_l = \rho_0\left[1 - \beta(\theta + \zeta z)\right]. \tag{7}$$

2.2. Mass conservation for the liquid phase

Although volume gas fractions may be significant at the well head, it is assumed that they reach low values rapidly so that $\alpha_l = 1 - \alpha_b \approx 1$ and (1) can be written as

$$\nabla \cdot \tilde{\mathbf{u}}_l \approx 0, \tag{8}$$

where the validity of the above can be assessed by adding the mass conservation for the two phases

$$\nabla \cdot \left(\alpha_l \tilde{\mathbf{u}}_l\right) + \nabla \cdot \left(\alpha_b \tilde{\mathbf{u}}_b\right) = 0. \tag{9}$$

Rearranging terms and assuming bubbles slip only in the vertical, (9) becomes

$$\nabla \cdot \tilde{\mathbf{u}}_l \approx -w_s \frac{\partial \alpha_b}{\partial z}. \tag{10}$$

Typical DwH plume velocities were $\mathcal{O}(1\,\mathrm{m\,s^{-1}})$ (McNutt et al., 2011) and the plume lateral scales were meters. Bubble volume fractions reduce from 0.5 to very small values over a few hundred meters, so a conservative estimate of the scale error implied by the above is

$$\frac{w_s \alpha_{b,z}}{\nabla \cdot \tilde{\mathbf{u}}_l} \approx \frac{0.2\,\mathrm{m\,s^{-1}}\,0.5}{200\,\mathrm{m}}\,\frac{10\,\mathrm{m}}{1\,\mathrm{m\,s^{-1}}} = .05 \ll 1. \tag{11}$$

2.3. Seawater momentum

Summing the momentum equations for each phase yields

$$\frac{D}{Dt}\left(\alpha_l\rho_l\tilde{\mathbf{u}}_l\right)+\frac{D}{Dt}\left(\alpha_b\rho_b\tilde{\mathbf{u}}_b\right)=-\nabla p+\nabla\cdot\alpha_l\boldsymbol{\tau}_l+\nabla\cdot\alpha_b\boldsymbol{\tau}_b+\alpha_l\rho_l\mathbf{g}+\alpha_b\rho_b\mathbf{g}, \tag{12}$$

where by definition $\Sigma_k\mathbf{M}_k=0$. Assuming that bubbles carry a negligible amount of momentum, reflecting their very small masses relative to seawater, (12) can be approximated as

$$\frac{D}{Dt}\left(\alpha_l\rho_l\tilde{\mathbf{u}}_l\right)=-\nabla p+\nabla\cdot\alpha_l\boldsymbol{\tau}_l+\alpha_l\rho_l\mathbf{g}. \tag{13}$$

Adopting a traditional Boussinesq approach given that $\rho_l'/\rho_0=(1-\alpha_b)\beta(T-T_0)\lesssim 0.15$, the final seawater momentum equations read

$$\rho_0\frac{D\tilde{\mathbf{u}}_l}{Dt}=-\nabla p+\rho_0\mathbf{g}+\nabla\cdot\boldsymbol{\tau}_l-\underbrace{\alpha_b\rho_0\mathbf{g}}_{bubble}-\underbrace{\rho_0\beta(T-T_0)\mathbf{g}}_{thermal}, \tag{14}$$

where the term $\alpha_b\rho_l'=-\alpha_b\rho_0\beta(T-T_0)$ has been neglected ($|\alpha_b\rho_l'|/\rho_0\lesssim 2\%$).

Introducing our temperature decomposition, (14) becomes

$$\rho_0\frac{D\tilde{\mathbf{u}}_l}{Dt}=-\nabla\tilde{p}+\nabla\cdot\boldsymbol{\tau}_l-\underbrace{\alpha_b\rho_0\mathbf{g}}_{bubble}-\underbrace{\rho_0\beta\theta\mathbf{g}}_{thermal}, \tag{15}$$

where the pressure term has been redefined as $\nabla\tilde{p}=\nabla p-\rho_0\mathbf{g}(1-\beta\zeta z)$.

Note that in (15) there are two contributions to the buoyancy force, one due to the presence of bubbles (*bubble*) and another one due to temperature gradients in the liquid phase (*thermal*).

2.4. Gas slip velocity

Momentum conservation (2) for gas is

$$\frac{D}{Dt}\left(\alpha_b\rho_b\tilde{\mathbf{u}}_b\right)=\nabla\cdot\alpha_b\boldsymbol{\tau}_b-\alpha_b\left(\nabla\tilde{p}+\rho_0\mathbf{g}-\rho_0\mathbf{g}\beta\zeta z\right)+\alpha_b\rho_b\mathbf{g}-\mathbf{M}_b, \tag{16}$$

where the term $\rho_0\mathbf{g}\beta\zeta z$ is negligible ($\frac{\rho_0 g\beta\zeta z}{\rho_0 g}\approx 3\times10^{-4}$ for $\zeta=0.05\,\mathrm{K\,m^{-1}}$ and $z=30\,\mathrm{m}$ which is the extent of the computational domain considered here). Note the explicit appearance of the interphase momentum transfer $\mathbf{M}_k$ in (16).

Neglecting bubble inertia (consistent with their small mass) and internal gas friction, (16) can be approximated by

$$\mathbf{M}_b=-\alpha_b\rho_0\mathbf{g}. \tag{17}$$

Gas/seawater momentum exchange is typically modeled using a drag law (Yapa and Dissanayake, 2012), i.e.

$$\mathbf{M}_b=-\frac{3}{4}\alpha_b\rho_0\frac{C_D}{d_b}\tilde{\mathbf{u}}_s\left|\tilde{\mathbf{u}}_s\right|, \tag{18}$$

where C_D is the drag coefficient and d_b is bubble diameter. With $C_D=0.47$ for an sphere in a turbulent flow (Roos and Willmarth, 1971) and $d_b=2\,\mathrm{mm}$,

$$w_s=\sqrt{\frac{4gd_b}{3C_D}}\approx 0.23\,\mathrm{m/s} \tag{19}$$

which is in agreement with the experimental slip velocities reported in Simiano (2005) and, importantly, with the typical values for the DwH (Socolofsky et al., 2011). Given the large Reynolds number expected at the inlet for deep water blowouts it is reasonable to assume here a uniform bubble distribution and therefore a unique slip velocity value (Lima Neto et al., 2008b). The above replaces the momentum equation for the second phase, a considerable simplification and practical computational aid.

2.5. Mass conservation of gas

The mass conservation for gas is

$$\frac{\partial}{\partial t}\alpha_b\rho_b+\nabla\cdot\left(\alpha_b\rho_b\tilde{\mathbf{u}}_b\right)=0, \tag{20}$$

where the gas phase velocity can be written as $\tilde{\mathbf{u}}_b=\tilde{\mathbf{u}}_l+\tilde{\mathbf{u}}_s+\tilde{\mathbf{u}}_d$ where $\tilde{\mathbf{u}}_d$ is the drift velocity (Simonin and Viollet, 1990). This term has been used to account for the interaction between bubbles and the influence of the liquid phase turbulence that is missed in the single bubble in a stagnant fluid model in (18). By rewriting $\tilde{\mathbf{u}}_d$ using the classical turbulent viscosity approach one may parametrize this enhanced turbulent transport due to the presence of bubbles. However such closures are still far from being conclusive (Sokolichin et al., 2004).

In this work the bubble model was intended to be kept as simple as possible and no parametrization for additional turbulent transport has been used. Therefore, the gas phase slip $\tilde{\mathbf{u}}_b$ is simply approximated as

$$\tilde{\mathbf{u}}_b=\tilde{\mathbf{u}}_l+\tilde{\mathbf{u}}_s-\mathcal{D}_b\frac{\nabla\alpha_b}{\alpha_b}, \tag{21}$$

where $\mathcal{D}_b$ is taken to be a constant diffusivity coefficient and (20) yields

$$\frac{\partial\alpha_b}{\partial t}+\nabla\cdot\left(\alpha_b\tilde{\mathbf{u}}_l\right)=\mathcal{D}_b\nabla^2\alpha_b-w_s\frac{\partial\alpha_b}{\partial z}. \tag{22}$$

2.6. Energy conservation

The seawater temperature equation is

$$\frac{\partial T}{\partial t}+\nabla\cdot\left(T\tilde{\mathbf{u}}_l\right)=\mathcal{D}_\theta\nabla^2T, \tag{23}$$

where $\mathcal{D}_\theta$ is taken to be a constant diffusivity coefficient. The diffusivity and slip velocity are the only differences between the two active scalars T and α_b, although molecular diffusion will be demonstrated to have a negligible impact. Using the decomposition in (6), (23) yields

$$\frac{\partial\theta}{\partial t}+\nabla\cdot\left(\theta\tilde{\mathbf{u}}_l\right)=\mathcal{D}_\theta\nabla^2\theta-w_l\,\zeta\,. \tag{24}$$

The transport equations can be then non-dimensionalized using a velocity, length and temperature scales U_s, L_s and θ_s respectively. Denoting non-dimensionalized variables using the same symbols as the dimensional ones above, the final set of transport equations may be written

$$\nabla\cdot\tilde{\mathbf{u}}_l=0, \tag{25}$$

$$\frac{D\tilde{\mathbf{u}}_l}{Dt}=-\nabla\tilde{p}+\frac{1}{Re}\nabla^2\tilde{\mathbf{u}}_l+Ri_b\alpha_b\hat{\boldsymbol{k}}+Ri_\theta\theta\hat{\boldsymbol{k}}, \tag{26}$$

$$\frac{\partial\alpha_b}{\partial t}+\nabla\cdot\left(\alpha_b\tilde{\mathbf{u}}_l\right)=\frac{1}{Pe_b}\nabla^2\alpha_b-w_s\frac{\partial\alpha_b}{\partial z}, \tag{27}$$

$$\frac{\partial\theta}{\partial t}+\nabla\cdot\left(\theta\tilde{\mathbf{u}}_l\right)=\frac{1}{Pe_\theta}\nabla^2\theta-w_l\,\zeta^*. \tag{28}$$

The non-dimensional parameters are the Reynolds number, $Re=U_sL_s/\nu$, the bubble and thermal Péclet numbers, $Pe_b=U_sL_s/\mathcal{D}_b$ and $Pe_\theta=U_sL_s/\mathcal{D}_\theta$ respectively, and the bubble and thermal Richardson numbers, $Ri_b=gL_s/U_s^2$ and $Ri_\theta=\beta\theta_s gL_s/U_s^2$ respectively. Finally, $\zeta^*=\zeta\,L_s/\theta_s$ is the non-dimensional stratification slope.

2.7. Model summary

Eqs. (25)–(28) form a closed set for computing the dynamic evolution of multiphase buoyant plumes driven by the density defect due to the presence of gas. Considering the mixture (liquid and dispersed bubble phase) momentum eliminates the need for explicit models of interphase stresses. Due to the very large difference in liquid and gas densities, the contribution of the gas phase to the mixture momentum can be neglected and, following the Boussinesq assumption (strictly valid only for small inlet gas volume fractions), density fluctuations due to bubbles appear only as a buoyancy force (Sokolichin et al., 2004). As such, the liquid phase velocity is non-divergent and closure requires an evolution equation for the gas phase volume fraction. The gas phase continuity equation can be written in terms of the computed liquid velocity and the relative (slip) velocity between the phases. For bubble flows (plumes, bubblers and aeration columns), the value of this parameter is typically found from semi-empirical fitting of the terminal rise velocity of single bubbles (Kuwagi and Ozoe, 1999; Schwarz and Turner, 1988; Sokolichin et al., 2004; Tomiyama, 1998). Since the rise velocity depends primarily on bubble size, the slip velocity is assumed constant for mono-disperse bubble distributions, consistent with experimental observations (Simiano, 2005).

The major limitations of the model for investigating deepwater blowouts involve (a) the need for relatively small values of inlet gas volume fraction (the Boussinesq assumption) and (b) the lack of explicit physico-chemical processes (constant slip velocity or constant, monodisperse bubble size). Although observations from the DwH incident have estimated gas volume fractions as high as 50% at the inlet (McNutt et al., 2011), intense entrainment will lead to rapid decay of the scalar. In addition, assuming incompressibility of the gas phase, strict validity of the Boussinesq approximation requires only that the vertical gradient of the gas volume fraction be small (see Eq. (11)). As such, we expect this model assumption to be reasonable at small downstream distances, in fully-developed plumes for even larger values of inlet gas volume fraction then those considered here.

Modelling the slip velocity as a single constant implies a monodisperse and constant bubble size distribution. In the absence of consumption and dissolution, individual gas bubbles should expand while rising, leading to an increased slip velocity. Very deep in the fluid, this expansion is extremely slow to occur. For example, moving from 1500 m to 1000 m involves a radial expansion of roughly 10%. Of course, there really is some degree of consumption and dissolution, so the actual expansion would be reduced. In a sense, a constant slip velocity roughly parameterizes consumption, dissolution and gas compressibility. The value of the slip velocity used here is consistent with experimental values for bubble sizes $\sim 2\,\text{mm} \le d_b \le \sim 8\,\text{mm}$ and corresponds to estimates previously used for the DwH plume (Socolofsky et al., 2011).

2.8. Integral models

Buoyant plumes and jets have been extensively studied using integral solutions first derived by Morton et al. (1956) and later extended to bubble plumes by Milgram (1983) and others. In these solutions the entrainment per unit length into the edge of the plume is characterized by representative local velocity and length scales, $\overline{W}(z)$ and $b(z)$ respectively, so that $(rU)|_\infty = -\alpha\, b\, \overline{W}$ where α is the entrainment coefficient and U and W are mean radial and vertical velocity components respectively.

Assuming Gaussian profiles for the mean vertical velocity $W(r,z) = \overline{W}(z)e^{-(r^2/b(z))^2}$, the volume, momentum and buoyancy flux, Q, M and B respectively, can be written as

$$Q = \int_0^\infty W r\, dr = \frac{1}{2} b^2 \overline{W}, \tag{29}$$

$$M = \int_0^\infty W^2 r\, dr = \frac{1}{4} b^2 \overline{W}^2, \tag{30}$$

$$B = \int_0^\infty W g' r\, dr = B_\theta + B_b, \tag{31}$$

where $g' = g\,\Delta\rho/\rho_0$ is the reduced gravity, g is the gravity acceleration and $\Delta\rho = \rho_e - \rho$ where $\rho_e(z) = \rho_0(1 - \beta\zeta z)$ is the unperturbed environment density profile and ρ is the density in the plume. This term can be rewritten as $\Delta\rho/\rho_0 = \beta\theta + \alpha_b - \alpha_b\,(\rho_b - \rho_l')\,/\rho_0$ where the last term, following previous approximations, has been neglected.

Thus, the thermal B_θ and bubble B_b buoyancy fluxes are defined as

$$B_\theta = \int_0^\infty W g\, \beta \Theta r\, dr, \tag{32}$$

$$B_b = \int_0^\infty W g\, \langle\alpha_b\rangle r\, dr, \tag{33}$$

where $\Theta = T - (T_0 + \zeta z)$ is the mean temperature perturbation (obtained by subtracting the stratification mode) and $\langle\alpha_b\rangle$ is the mean gas volume fraction. Gaussian profiles are also assumed for $\Theta = \overline{\Theta}(z)\exp(-r^2/b(z)^2)$ and $\langle\alpha_b\rangle = \overline{\alpha_b}(z)\exp(-r^2/(\lambda\, b(z))^2)$ where the parameter λ is the ratio of the gas volume fraction to momentum plume widths.

Using the previous definitions and the transport equations described in Section 2, the integral model equations read

$$\frac{dQ}{dz} = 2\alpha M^{1/2}, \tag{34}$$

$$\frac{dM}{dz} = \frac{1}{\gamma}\frac{Q}{M}\left(B_\theta + \frac{\lambda^2+1}{2} B_b\right), \tag{35}$$

$$\frac{dB_\theta}{dz} = -N^2 Q, \tag{36}$$

$$\frac{dB_b}{dz} = -g\frac{d}{dz}\int_0^\infty w_s \alpha\, r dr, \tag{37}$$

where γ is the momentum amplification factor defined as the ratio of the total momentum flux to the momentum flux carried by the mean flow and N is the buoyancy frequency defined as $N = \sqrt{-(g/\rho_0)\,\partial\rho_e/\partial z} = \sqrt{\beta\, g\, \zeta}$.

For $w_s \neq 0$, the system in (34)–(37) is unclosed. While this has been circumvented by hydrostatic assumptions (Ditmars and Cederwall, 1974), even a constant slip velocity breaks self-similarity in the same way as a non-zero stratification. When $w_s/w_0 \ll 1$, the gas phase contribution can be ignored as in Cardoso and McHugh (2009) and the system defined by Eqs. (34)–(37) is closed ($B_{b,z} = 0$). Note that in the integral models (Eqs. (34)–(37)) the effect of bubbles on the turbulence is only accounted in the momentum Eq. (35) through the γ parameter which is known to be larger in multiphase plumes due to turbulent mixing enhancement associated to the presence of a gas phase (Milgram, 1983). Thus, the turbulent transport of temperature or gas volume fraction is not explicitly accounted in Eqs. (36) and (37). However, even for single phase plumes in unstratified environments ($\zeta = 0$), where the integral solutions would predict a constant buoyancy flux B ($B_{,z} = 0$), this value should actually decrease due to the turbulent mixing.

3. Computational test case

3.1. Plume parameters

We consider three plumes differentiated only by the ratio of active scalar contributions to the inlet buoyancy flux: a purely thermal, a (almost) purely bubble and a hybrid case. In each case, the inlet buoyancy

Table 1
Summary of the cases.

Case	Plume description	δ	$\alpha_{b,0}$	$\Delta T_0(K)$
T	Thermal	1	–	746
B	Bubble	0.05	0.142	37
H	Hybrid	0.5	0.075	373
H2	Hybrid 2	0.9	0.015	671

flux is fixed to the order of magnitude estimated for the DwH spill, $B_{DwH} = g\,\Delta\rho_0\,w_0 A/\rho_0 = 0.37\,\mathrm{m^4\,s^{-3}}$, where $D = 0.5$ m is the source diameter, $w_0 = 1.3\,\mathrm{m\,s^{-1}}$ is the inlet liquid phase velocity and $A = \pi\,D^2/4 \approx 0.2\,\mathrm{m^2}$ is the inlet cross section area. This is thermally equivalent to $B_0 = \rho_0\,C_p B_{DwH}/(\beta\,g) = 0.8$ GW, where $C_p = 4{\times}10^3\,\mathrm{J\,kg^{-1}\,K^{-1}}$ is the heat capacity of sea water.

This fixed inlet buoyancy flux B_{DwH} can be distributed over either or both of the thermal δB_θ^0 and gas phase $(1-\delta)B_b^0$ fractional contributions where $B_\theta^0 = gAw_0\beta\,\Delta T_0$ and $B_b^0 = gAw_0\alpha_{b,0}$. $\alpha_{b,0}$ is the gas volume fraction at the inlet and ΔT_0 is the inlet temperature difference with respect to the seafloor reference state. Here the gas phase buoyancy flux is the *dynamic* flux based on the liquid phase velocity, w, in contrast to the *kinematic* flux based on $(w + w_s)$. This ensures that the input momentum forcing is identical for all plumes. Table 1 summarizes the three cases studied: bubble (B), hybrid (H) and thermal (T). An additional case (H2), with only 10% of the buoyancy flux due to the presence of bubbles, has also been considered to gain more insight on the dependency of the turbulence enhancement on the inlet gas volume fraction. To match expectations in a deep-water release, the effluent in all cases is substantially warmer than the ambient fluid.

3.2. Computational model

The transport equations, (25)–(28) are solved using the spectral element method (SEM) code Nek5000 (Fischer et al., 2008). This code has been validated for a wide range of flow configurations and has demonstrated excellent scalability on parallel machines. SEM overcomes the limitation of the classic fully-spectral methods in terms of restricted type of boundary conditions and geometry allowing high-order solutions for complex grids (Deville et al., 2002).

Here we make use of the spectral accuracy and scalability of Nek5000 to perform highly resolved simulations. Instead of a typical LES approach explicitly modelling subgrid scales via variations of Smagorinsky eddy diffusivities (Özgökmen et al., 2009a; 2009b), we use the spectral vanishing viscosity (Karamanos and Karniadakis, 2000) technique where the near-grid scale coefficients of the spectral polynomial expansion are progressively filtered (Deville et al., 2002; Fischer and Mullen, 2001). This is equivalent to increasing the nominal Reynolds and Péclet numbers only at near-grid scales. Specifically, the current results use a 5% polynomial filtering of the two highest modes in the 12th order Legendre expansion for all computed fields. This procedure preserves the exponential convergence of the spectral solver while avoiding the cost of computing SGS coefficients. Results using this approach in the context of turbulent channel flow show excellent agreement with DNS, relative insensitivity to the filter shape and overall computational efficiency (Koal et al., 2012).

The computational domain, shown in Fig. 1, is a cylinder of radius $R/D = 25$ and height $L_z/D = 60$ ($R = 12.5$ m and $L_z = 30$ m). The domain is decomposed into $K = 12544$ elements and the solution on each element is approximated using 12th order Legendre polynomials for a total number of degrees of freedom, $N_T \approx 22$ million. Typical spatial resolution near the axis of the plume is 0.02 m increasing to 0.3 m in radial far-field.

Dirichlet boundary conditions specifying top hat profiles of velocity and scalar fields at the circular inlet are implemented on the lower boundary. On lateral boundaries, perturbation temperature and gas volume fraction are set to zero. To allow the entrainment of fresh

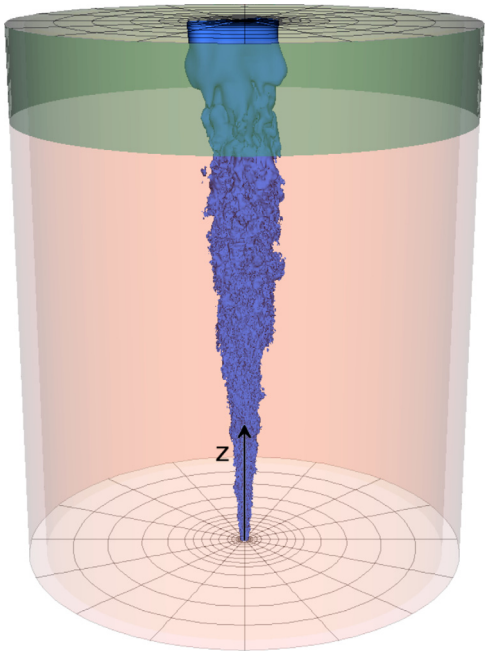

Fig. 1. A sketch of the computational domain showing an instantaneous isosurface of vertical velocity extending over the domain. The mesh at $z = 0$ shows the boundaries of the spectral elements. Top and lateral shaded areas show the approximate extent of the numerical sponges.

fluid into the domain, open boundary conditions are used for the momentum on the sides. Similar conditions, imposed at the top, allow dynamic outflow of the plume. To smooth fluctuations in the fields in the vicinity of the open boundary conditions, numerical sponges are implemented over $r/D \geq 20$ and $z/D \geq 42.5 = z_{\max}$. The region of interest (ROI), defined as the unperturbed computational domain, extends over $z/D \leq 42.5$ and $r/D \leq 20$. To ensure that the sponges do not alter results in the ROI, a comparison between the domain described above and one extended to $z/D = 80$ in the vertical was performed and resulted in no significant differences.

Table 2 shows the set of parameters used in this work. The velocity U_s, length L_s and temperature θ_s scales are set to be the injection velocity w_0, the pipe diameter D and the bottom to top background seawater temperature difference ($\theta_s[\mathrm{K}] = \zeta\,z_{\max}\,L_s$) respectively. For each case in Table 1 the flow was evolved in time until steady values of volume integrated quantities (total scalar mass as well as the kinetic and potential energies) were achieved.

For all cases the initial conditions were zero velocity and scalar (α, θ) fields. Once the flow was fully developed, statistics were computed by averaging in time over a period $\Delta\tau = 250D/w_0$. For the axisymmetric plumes, statistical sampling was increased by additional averaging over $N_\phi = 200$ azimuthal points. Longer time samplings did not exhibit significant differences for the mean and second order quantities considered. The simulations were carried out on a Cray XE6 using 960, 2.2 GHz AMD Magny-Cours cores. The CPU time to achieve the reported statistical sampling was approximately 300,000 core hours for each case.

4. Results

The plumes are forced by identical inlet momentum and buoyancy fluxes. Consequently, any observed differences between the evolution of single and multiphase plumes is entirely due to the slip velocity of the gas phase. In the present cases, the imposed slip velocity is only 18% of the injection velocity w_0, and an even smaller percentage of the maximum vertical velocity produced by the large buoyancy flux. The comparisons, therefore, minimize the differences between the three

Table 2
Plume simulation parameters.

w_0 (m/s)	D (m)	θ_s (K)	w_s (m/s)	w_s/w_0	Re	Pr	Sc	Ri_b	Ri_θ	$\zeta*$
1.3	0.5	1.062	0.23	0.18	13,000	7.0	1.0	2.9	6.2×10^{-4}	0.023

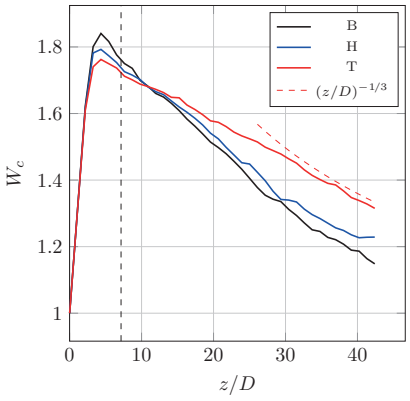

(a) Mean centerline velocity

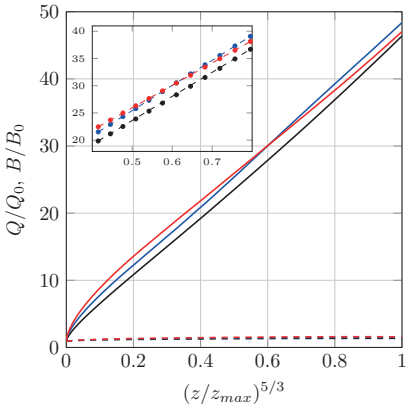

(b) Volume flux

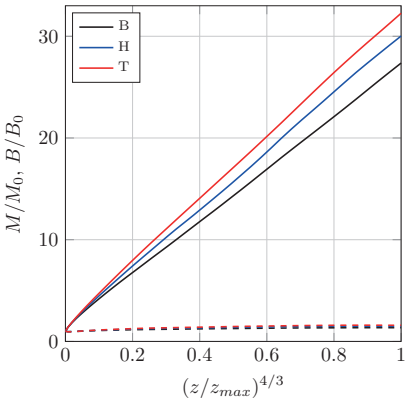

(c) Momentum flux

Fig. 2. (a) Mean centerlines vertical velocity component W_c for the bubble (case B, black line), thermal (case T, red line) and hybrid (case H, blue line) plumes. $z = 5\,L_M$ is indicated as a vertical dashed line. Self-similar solution $W_c \sim z^{-1/3}$ shown as a thin red dashed line. (b) Volume (solid lines) and buoyancy (dashed lines) fluxes for the three cases using the thermal plume scaling, $W_c \sim z^{-1/3}$ where $z_{\max}/D = 42.5$. The inset shows a detail of the turnover point in Q for the thermal and hybrid cases. Slope indicated as thin dashed lines. (c) Momentum (solid lines) and buoyancy (dashed lines) fluxes as in (b). (For interpretation of the references to color in this figure legend, the reader is referred to the web version of this article.)

cases; the three plumes are essentially identical and the sole differential parameter is small in relative terms. This parameter appears only in the conservation equation for the gas phase volume fraction. As we shall show, the difference in the values of the modeled molecular diffusivity of the two scalars is insignificant given the predominance of turbulent mixing.

With the instantaneous velocity components given by $(\tilde{u}, \tilde{v}, \tilde{w})$ in cylindrical polar coordinates (r, θ, z), upper case letters or angle brackets $\langle\cdot\rangle$ denote combined temporal and azimuthal averages and lower case letters denote fluctuating quantities; the classic Reynolds decomposition reads, $\tilde{\mathbf{u}} = \mathbf{U} + \mathbf{u}$. For dimensional consistency, the active scalar field, s is defined as $s \equiv \beta\,\theta + \alpha_b$.

4.1. Mean transport

The mean centerline vertical velocity W_c is shown in Fig. 2(a) for the three cases described in Table 1. Close to the source the momentum flux at the inlet generates a buoyant jet that rapidly evolves into a buoyant plume. The transition location can be estimated using the Morton length scale $L_M = M_0^{3/4} B_0^{-1/2} = 1.43D$. Shabbir and George (1994) observed that the buoyant plume is established at $z/L_M > 5$ shown in Fig. 2(a) as a dashed line.

Given identical values of the significant inlet momentum flux and the disparity between the slip and inlet velocities, the maximum vertical velocity in each case occurs at the same downstream location, $z/D \approx 4$. The effect of the slip velocity, however, is seen even at this small distance where the maximum value of vertical velocity increases with increasing gas volume fraction. Beyond this maximum, the vertical velocity in both multiphase plumes decays significantly faster than in the single-phase case. Despite a nearly 50% decrease in inlet gas volume fraction, the decay rate in the hybrid plume closely mimics that of the bubble plume. The rapid increase in the decay rate of the centerline velocity suggests that the presence of gas, as modeled here, has a significant impact on the mixing of momentum in the plume.

The downstream evolution of the primary prognostic integral model quantities, the radially averaged volume and momentum fluxes, are show in Fig. 2(b) and (c). For comparison, each flux is

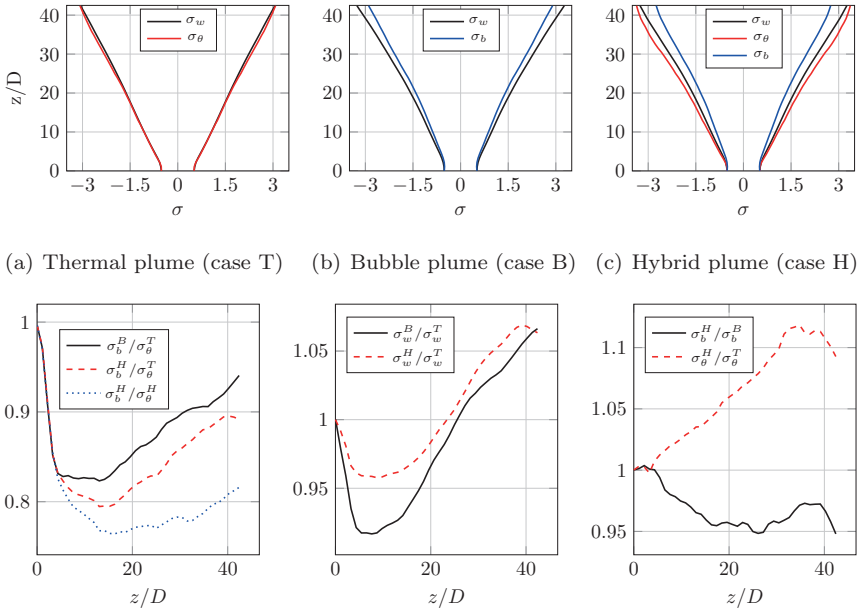

(a) Thermal plume (case T) (b) Bubble plume (case B) (c) Hybrid plume (case H)

(d) Scalar plume width ratios. (e) Momentum plume widths ratios. (f) Hybrid to *pure* plume width ratios.

Fig. 3. Top: Thermal (left), bubble (center) and hybrid (right) plumes momentum and scalar widths. Bottom: Selected plume widths ratios.

plotted against $(z/z_{\max})^{a_i}$ where $a_Q = 5/3$ and $a_M = 4/3$ are the standard, self-similar values for an unstratified thermal plume. Although non-zero stratification and slip velocity prevent strict self-similar evolution of the integral fluxes, for the present parameter values and vertical domain, the vertical variation in the buoyancy flux (shown by dashed lines in both rescalings) is small in all cases. The rescaled Q and M fluxes are nearly linear for $z/D > 20$. $(z/z_{\max})^{5/3} \gtrsim 0.3$ and $(z/z_{\max})^{4/3} \gtrsim 0.35$ respectively.

Fig. 2(b) indicates that the vertical volume flux, and hence the horizontal entrainment, is initially larger in the single phase plume. However, farther downstream both multiphase plumes show greater, and nearly identical, slopes relative to the thermal case. This increase in Q is seen despite the clear decrease in the growth rate of the momentum flux shown in Fig. 2(c). As such, in terms of typical integral model parameterizations, the multiphase plumes exhibit larger values, with respect to the thermal plume, of both the entrainment coefficient, α and the momentum amplification factor, γ.

While W, Θ and $\langle\alpha_b\rangle$ are not strictly self similar, each quantity is extremely well fit by Gaussian profiles at any vertical location beyond $z/D \gtrsim L_M/D$. Closer to the source, the imposed top-hat profiles persist. The (half-)width of a general quantity ψ is defined using the standard deviation, σ, in $\psi(r,z) = \psi_c(z)\exp(-r^2/\sigma_\psi^2(z))$ where r is the radial coordinate and $\psi_c(z)$ is the centerline value.

The radial extent of both the momentum and scalar fields in the three cases is shown in the top row of Fig. 3 using best-fit σ values for momentum (black), gas volume fraction (blue) and temperature (red). In the single phase case, temperature advects with the fluid and the momentum and scalar plumes necessarily grow at the same rate. In the absence of stratification, the growth is linear. For multiphase plumes, $\langle\alpha_b\rangle$ is stretched with respect to the momentum in the direction of the slip velocity. This narrowing of the bubble plume is seen in both multiphase cases where the half-widths of $\langle\alpha_b\rangle$ are less than those of W for all values of z. The decrease of the width of the bubble plumes relative to the single phase thermal plume is shown in Fig. 3(d). Both multiphase plumes are initially narrower than the thermal plume. Downstream, $z/D \gtrsim 15$, however, the ratio increases with the same, nearly constant, slope for both the bubble and hybrid cases. Assuming this trend persists, one would expect that the multiphase scalar plumes, despite the narrowing effects of the slip velocity, would eventually be broader than the single phase thermal plume.

The narrowing of the buoyancy source by the slip velocity in the multiphase plumes also changes the evolution of the momentum fields. In contrast to the single phase case, the top panel shows nonlinear evolution of both scalar and momentum plume widths in the bubble and hybrid cases. The effect of the slip velocity on the dynamics is quantified by plotting the ratio of the multi to single phase momentum plume widths in Fig. 3(e). In the very near-field, the decrease in the radial extent of $\langle\alpha_b\rangle$ effectively reduces the width of multiphase momentum plumes relative to the single phase results. This initial reduction is compensated downstream by an apparent increase in turbulent mixing resulting in more rapid radial spreading of momentum in the multiphase plumes.

As any deep-water release will necessarily involve the combined effects of multiple buoyancy components, it is instructive to examine the differences in the evolution of the two active scalar fields in the present hybrid case. As shown in Fig. 3(d), the ratio of the bubble to thermal plume widths in the hybrid case decreases rapidly in the near-field at exactly the same rate as $\sigma_b^B/\sigma_\theta^T$. Unlike the $\sigma_b^B/\sigma_\theta^T$ ratio, $\sigma_b^H/\sigma_\theta^H$ does not show a rapid downstream increase and the bubble plume is always narrower than the thermal plume in the hybrid case (Fig. 3(c)). The momentum, due to equal contributions from each scalar, is necessarily confined between the two scalar plumes. Comparisons of the width of the hybrid scalar plumes $(\sigma_b^H, \sigma_\theta^H)$ to their 'pure' counterparts $(\sigma_b^B, \sigma_\theta^T)$ are shown in Fig. 3(f). The enhanced mixing in the hybrid case with respect to the purely thermal plume results in faster spread of the temperature field in the presence of a gas phase. In contrast, the σ_b^H/σ_b^B ratio is approximately constant for $z/D \gtrsim 15$ reflecting the near uniform vertical offset in the scalar width ratios seen in Fig. 3(d).

As indicated by the vertical evolution of the integral fluxes Q and M, the presence of a gas phase increases the entrainment flux, reduces the momentum growth rate through the momentum amplification factor γ and implies a non-unitary value of the plume width parameter $\lambda = \sigma_s/\sigma_w$. Fig. 4(a) shows the entrainment coefficient α for the

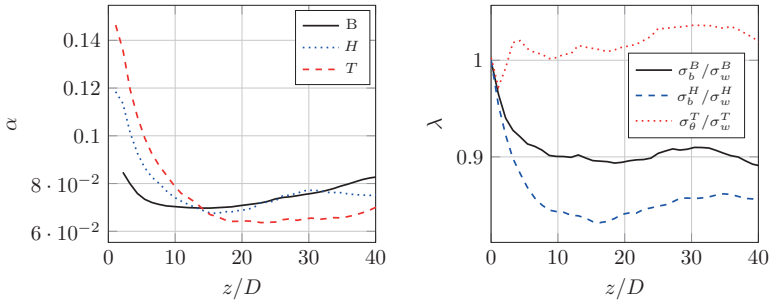

(a) Entrainment coefficient (b) Scalar to momentum plume width ratio

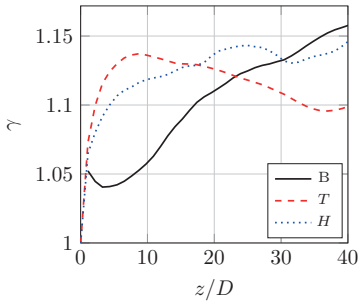

(c) Momentum amplification factor

Fig. 4. (a) Entrainment coefficient α. (b) Scalar to momentum plume width ratio λ. (c) Momentum amplification factor γ.

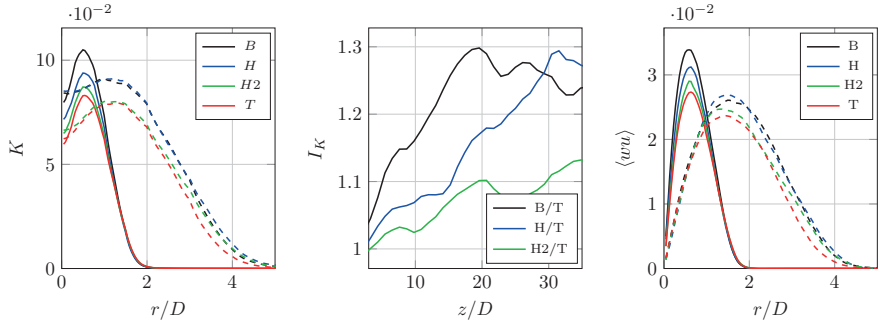

(a) TKE (b) Radially integrated TKE ratios (c) Reynolds stress $\langle wu \rangle$

Fig. 5. (a) Turbulent kinetic energy at $z/D = 10$ (solid lines) and $z/D = 31.5$ (dashed lines) for the cases in Table 1. (b) $I_K(z/D)$ for cases B, H and H2 with respect to the single phase case. (c) Reynolds stress $\langle wu \rangle$ as in (a).

three plumes computed using (34). The evolution of Q, with an initial faster growth for the single phase plume, results in larger values of α for $z/D \lesssim 12$. However, farther downstream, multiphase plumes exhibit larger dQ/dz associated with increased entrainment fluxes. Similar values of dQ/dz for the bubble and hybrid cases lead also to similar entrainment coefficients in the ROI.

Using the best-fit values of σ, the vertical dependence of λ for the three plumes is shown in Fig. 4(b). As expected, λ is close to one for the single phase flow, but smaller for the bubble ($\lambda \sim 0.9$) and the hybrid ($\lambda \sim 0.85$) cases. While values in the range $0.4 \leq \lambda \leq 1$ have been used in multiphase integral models, the present values are consistent with those used by Milgram (1983) based on observations of a relatively large-scale, environmental bubble plume.

Distinct differences in the turbulence, as parameterized in integral models by the amplification factor γ defined in (35), are shown in Fig. 4(c). In the thermal case, the parameter grows rapidly and reaches an arguably constant value $\lambda \approx 1.1$ in agreement with previous results (Chen and Rodi, 1980; George et al., 1977). In the multiphase cases, γ values are initially smaller, with less vertical momentum carried by the turbulence due to the narrowing of the mean velocity field. Downstream, however, the turbulent contribution to the total momentum increases continually resulting in non-constant values of γ over the available vertical extent of the computations.

The results obtained for the mean vertical evolution of the modeled plumes agree with basic experimental observations, namely that the presence of gas enhances turbulent mixing and thus the spreading rates of bubble plumes. Parameterization of the gas phase through a simple slip velocity allows decoupling of the active scalar field from the momentum. This results in differences in the vertical evolution of the scalar and momentum plumes ($\lambda < 1$). The initial enhanced concentration of the buoyancy produces larger maximum vertical velocities but also generates increased turbulent transport and mixing resulting in faster spreading rates than in the single phase case.

Table 3
Ratios of some selected integral quantities for the bubble and hybrid cases with respect to the thermal case.

$\int_0^\infty \cdot r\,dr$	B		H		H2	
	$z/D = 10$	$z/D = 31.5$	$z/D = 10$	$z/D = 31.5$	$z/D = 10$	$z/D = 31.5$
K	1.16	1.24	1.07	1.29	1.02	1.11
$\langle wu\rangle W_{,r}$	1.23	1.06	1.12	1.09	1.03	1.02
$Ri_s\langle ws\rangle$	1.02	1.14	0.98	1.22	0.99	1.07

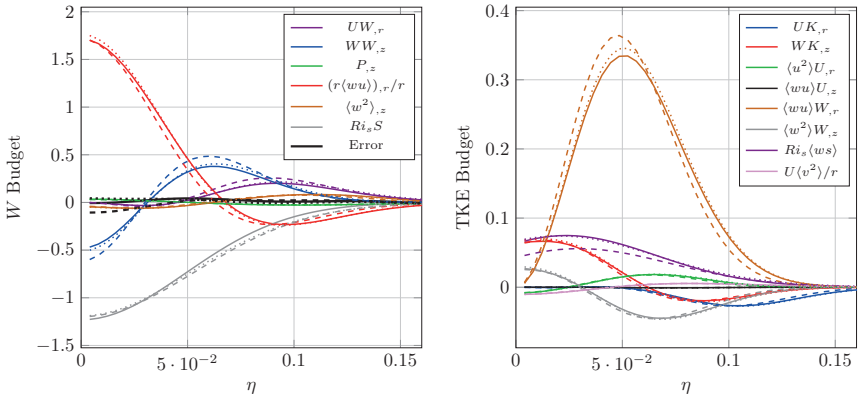

(a) W Budget (b) TKE Budget

Fig. 6. (a) Mean vertical momentum budget for the bubble (solid lines), hybrid (dotted lines) and thermal (dashed lines) plumes. (b) Turbulent kinetic energy budget as in (a).

4.2. Plume turbulence

Differences in the turbulence produced by the three plumes can be quantified by comparing the turbulent kinetic energy (TKE), $K = \frac{1}{2}\langle u_i u_i\rangle$, at two different vertical locations as shown in Fig. 5(a). At $z/D = 10$ (solid lines) the TKE increases with increasing inlet gas volume fraction. Defining the radial integral of K as $I_K = \int_0^\infty Kr\,dr$, the multiphase plumes B, H and H2 exhibit I_K increases of 16%, 7% and 2% respectively relative to the single phase case (see Table 3). The vertical location of the peak where the maximum value of TKE occurs is the same for all the cases. At $z/D = 31.5$ (dashed lines) the profile has widened but the peak still persists showing maximum values only slightly smaller than closer to the source. The increase in TKE in the multiphase plumes with respect to the thermal case is now larger; the hybrid and bubble cases, with similar values of TKE, are 24–29% larger respectively. For comparison, case H2 exhibits K values almost identical to the thermal case in the region close to the axis but the profile increases along the radial direction eventually becoming similar to that observed in the other multiphase plumes. With only 10% of the buoyancy flux due to bubbles, the I_K value in the H2 case is 11% larger than in the single phase plume.

Fig. 5(b) shows the vertical development of the ratio of multiphase I_K to the single phase case. The bubble plume, with the largest gas volume fraction, initially exhibits the fastest relative growth of I_K followed by an approximately constant plateau region. In the hybrid plume, the growth of K occurs at a slower rate over the entire computational domain. At the end of the ROI both bubble and hybrid cases exhibit similar values of I_K. For the H2 plume, I_K grows the slowest reaching values ~10% smaller than in the other two multiphase cases at the end of the computational domain. This suggests that the production of TKE with respect to the single phase plume depends strongly, and nonlinearly on the amount of gas at the inlet.

The presence of a gas phase, as modeled here, does not appreciably change the anisotropy of the turbulence. In all cases, $\langle w^2\rangle \approx 2\langle u^2\rangle \approx 2\langle v^2\rangle$, consistent with classical turbulence predictions for nearly parallel shear flows (Tennekes and Lumley, 1972). Comparisons of the Reynolds stresses, $\langle wu\rangle$, at the same vertical locations are shown in Fig. 5(c). The results are similar to those found for the TKE: close to the source the $\langle wu\rangle$ values are ordered according to gas content while farther downstream, bubble and hybrid plumes are very similar. Again, near the axis, the Reynolds stress in the small gas volume fraction case is similar to observations in the single phase plume but the profile approaches the other multiphase profiles as r increases. When compared to the thermal case, the bubble plume shows 16% and 24% increases in $\langle wu\rangle$ at $z/D = 10$ and $z/D = 31.5$ respectively, very close to the results for the TKE.

In summary, the proposed model, with no parametrized bubble induced turbulence (Sokolichin et al., 2004), predicts a local increase in TKE of up to ~30% in multiphase plumes compared to the single phase case. This difference is substantial, especially in light of the relatively small value of the slip velocity in the near field for the large inlet buoyancy flux considered. The results suggest that even small amounts of gas affect the turbulence in the plume and that the relationship between the inlet gas volume fraction and the resulting increase in the turbulent mixing is not linear.

4.3. Mechanism for enhanced two-phase turbulence

The mechanism by which the slip velocity enhances the turbulent production can be explained in the context of the TKE budget. Given the results shown in Fig. 2 we assume local self-similarity over a relatively narrow vertical extent, $30.4 < z/D < 39.1$. Rescaling the data using $\eta = r/z$, it is possible to evaluate the different contributions to the budgets of mean momentum, scalar and TKE.

Using this approach, results for the budget of mean vertical momentum,

$$U\frac{\partial W}{\partial r} + W\frac{\partial W}{\partial z} = -\frac{\partial P}{\partial z} - \frac{1}{r}\frac{\partial\left(r\langle uw\rangle\right)}{\partial r} - \frac{\partial\langle w^2\rangle}{\partial z} + Ri_\theta\theta + Ri_b\alpha_b, \qquad (38)$$

are shown in Fig. 6(a). The main contributions are the radial turbulent transport, the vertical mean advection and the buoyancy, in

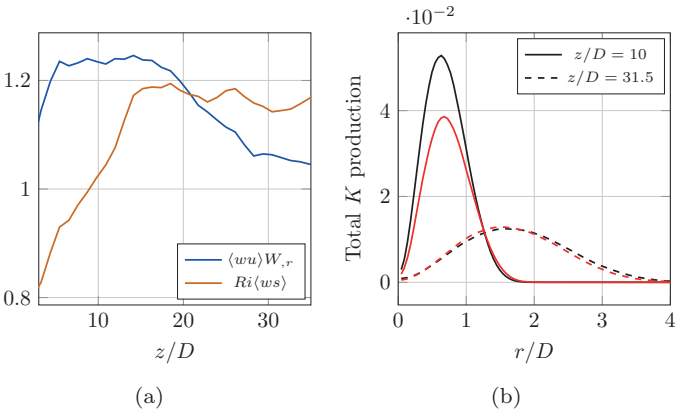

Fig. 7. (a) Bubble to thermal ratio of the mechanical (blue line) and buoyancy (orange line) production terms. (b) TKE production for the bubble (black line) and thermal (red line) at two different locations $z/D = 10$ (solid lines) and $z/D = 30.5$ (dashed lines). (For interpretation of the references to color in this figure legend, the reader is referred to the web version of this article.)

agreement with those reported in Shabbir and George (1994) for a thermal buoyant plume. The small error, shown as a thick black line, indicates that the local self-similar approximation is reasonable.

Fig. 6(b) shows the TKE budget

$$U\frac{\partial K}{\partial r} + W\frac{\partial K}{\partial z} = -\langle u^2\rangle\frac{\partial U}{\partial r} - \langle uw\rangle\frac{\partial U}{\partial z} - \langle uw\rangle\frac{\partial W}{\partial r} - \langle w^2\rangle\frac{\partial W}{\partial z} - \frac{U}{r}\langle v^2\rangle + Ri_\theta\langle w\theta\rangle + Ri_b\langle w\alpha_b\rangle - \epsilon - \omega, \quad (39)$$

where ϵ stands for dissipation and ω accounts for turbulence diffusion plus pressure strain terms which are not explicitly calculated. In all cases, the production of K is dominated by the mean shear (mechanical) contribution, $\langle wu\rangle W_{,r}$. While relatively larger in the presence of a gas phase, direct buoyancy production, $Ri_s\langle ws\rangle$, accounts for no more than 20% of the total in terms of radial integral quantities. At these vertical locations, the advection terms $UK_{,r}$ and $WK_{,z}$ are also significant. The results are in agreement with the experimental thermal plume budgets reported in Shabbir and George (1994).

In general, the differences between the plumes over the assumed self-similar extent are small in both budgets. In particular, the dominant mechanical TKE production term at $z/D \sim 35$ is only 6% larger in the bubble plume than in the thermal case (see Table 3). The smaller buoyancy contribution, accounting for only a fraction of the total, is 14% larger. The ~25% increase in I_K observed in Fig. 5(b) for $z/D \gtrsim 20$ must therefore result from larger turbulence production closer to the inlet. Fig. 7(a) shows the vertical dependence of the ratio of mechanical and buoyancy production between the bubble and thermal cases. In the region $5 \lesssim z/D \lesssim 18$ the mechanical production in the bubble case is ~24% larger than in the thermal plume. Farther downstream this ratio decays. The radially averaged direct buoyancy production is initially smaller in the bubble case due to the narrowing of the buoyancy source by the slip velocity. Downstream, however, there is a near constant ~18% increase in buoyancy production in the bubble plume.

Differences in the mechanical production of turbulence are due to the initial vertical stretching of the buoyancy forcing by the slip velocity. As shown in Fig. 8(a), at $z/D = 10$ the bubble plume exhibits larger shear close to the axis leading to larger production (Table 3). The turbulence is advected vertically resulting in larger downstream values of TKE. The enhanced conversion of mean to turbulent kinetic energy in the near field necessarily reduces the mean shear. However, the reduction of mean vertical velocity gradients is offset by the presence of larger Reynolds stresses. As such, by $z/D = 31.5$ the mechanical production in the bubble plume still exceeds that in the thermal case.

While the effects on the mechanical production are dominant, the increase in direct buoyancy production, $Ri_s\langle ws\rangle$, in the bubble plume can also be linked to the slip velocity. The production of $\langle ws\rangle$ is given by the turbulent scalar flux equations

$$\frac{D\langle w\alpha_b\rangle}{Dt} - \left(Ri_\theta\langle\theta\alpha_b\rangle + Ri_b\langle\alpha_b^2\rangle\right) + w_s\left\langle w\frac{\partial\alpha_b}{\partial z}\right\rangle + \epsilon_b = -\left[\langle u\alpha_b\rangle\frac{\partial W}{\partial r} + \langle uw\rangle\frac{\partial\langle\alpha_b\rangle}{\partial r}\right], \quad (40)$$

$$\frac{D\langle w\theta\rangle}{Dt} - \left(Ri_\theta\langle\theta^2\rangle + Ri_b\langle\theta\alpha_b\rangle\right) + \zeta^*\langle w^2\rangle + \epsilon_\theta = -\left[\langle u\theta\rangle\frac{\partial W}{\partial r} + \langle uw\rangle\frac{\partial\Theta}{\partial r}\right], \quad (41)$$

where ϵ_b and ϵ_θ account for the dissipation, turbulent diffusion and fluctuating pressure-scalar gradient correlations terms for bubbles and temperature respectively.

The two mean production terms in each equation, due to radial gradients in both the mean vertical velocity and the mean scalar field, are written the right hand side. Radial profiles of these terms are shown in Fig. 9 at $z/D = 21$. Both quantities are larger in the bubble case. The stretching of $\langle\alpha_b\rangle$ relative to Θ produces larger mean gradients as shown in Fig. 8(b). As a result, the relative contribution to

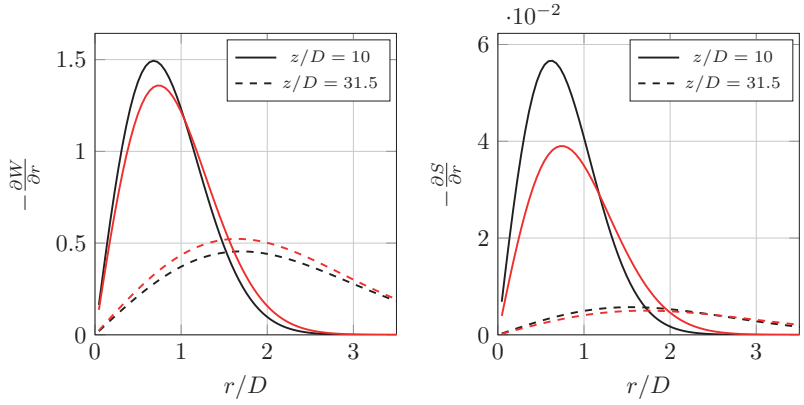

Fig. 8. Mean vertical velocity W (left) and scalar S (right) at $z/D = 10$ (solid lines) and $z/D = 30.5$ (dashed lines) for the bubble (black lines) and thermal (red lines) plumes. (For interpretation of the references to color in this figure legend, the reader is referred to the web version of this article.)

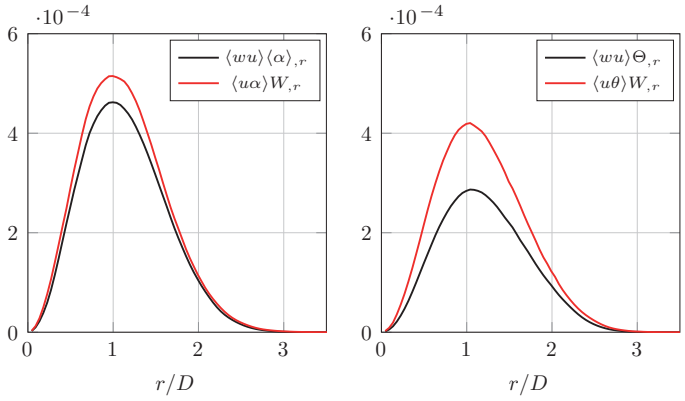

(a) Bubble plume (b) Thermal plume

Fig. 9. Buoyancy production contributions for the bubble (left) and thermal (right) plumes at $z/D = 21$.

the production of $\langle ws \rangle$ from the mean scalar gradient is considerably increased in the bubble case. Additionally, the stratification provides a negative-definite contribution to the production of $\langle w\theta \rangle$ while the slip velocity produces direct contributions to the production of $\langle w\alpha_b \rangle$ via the indefinite correlation $\langle w \frac{\partial \alpha_b}{\partial z} \rangle$.

5. Conclusions

It is well known that the presence of a gas in multiphase plumes increases turbulence mixing, entrainment and spreading rates with respect to single phase, thermal cases. Here, turbulence resolving computations are used to examine the mechanisms for this difference in dynamics and to quantify its extent in the context of deep water blowouts with inlet buoyancy fluxes much larger than those typically found in experiments. To clearly isolate the role of a dispersed gas phase on the dynamics, we derive a parsimonious bubble model directly from the governing equations under Boussinesq assumptions. The resulting model contains only a slip velocity as input and avoids any explicit parameterization of bubble-induced turbulence. Simplification of the system to a single momentum equation allows feasible explicit computations of the near-field turbulence over scale ranges commensurate with those of previous and potential deepwater releases.

Using this model, we compute the development of plumes in the idealized case of two, thermal and gas, buoyancy sources. As such any difference in the dynamics of single and multiphase plumes are due entirely to the slip velocity of the gas phase relative to that of the liquid. Comparing flows differentiated only by the ratio of buoyancy contributions at the inlet, modeled two-phase plumes are found to produce more turbulence, and thus spread faster than in the purely thermal case. Despite the simplicity of the model and the small value of the imposed slip velocity relative to that of the plume itself, differences in observed turbulence levels are significant. The relationship between the inlet gas volume fraction and the observed turbulence enhancement is highly non-linear. A 50% reduction in the inlet gas volume fraction produces no significant difference in the multiphase turbulent kinetic energy budgets. Appreciable differences between the single and multiphase plume in terms of turbulence intensities are observed even when gas-phase buoyancy contribution is only 10% of the total.

Explicit examination of kinetic energy budgets indicates that turbulent production is primarily due to mechanical shear while direct production from buoyancy sources is a minor contribution. Larger shear production in multiphase cases is associated with the vertical stretching induced by the gas phase slipping with respect to the liquid. When compared to a purely thermal plume, the dispersed gas phase necessarily narrows the mean momentum field relatively close to the inlet. This larger mean shear is responsible for the increased conversion of mean to turbulent energy responsible for larger entrainment and faster spreading downstream.

In the context of integral model formulations, the numerical experiments predict modest increases over purely thermal plumes for the entrainment coefficient and the expected increase in the ratio of momentum to scalar plume widths in the presence of a gas phase. The narrowing of the bubble plume with respect to the momentum plume is greater in the case of mixed buoyancy sources. The observed parameters are reasonably constant for $z/D \gtrsim 15$ with values falling within the (considerable) range of previous experimental measurements in isothermal bubble plumes. Consistent with the explicit quantifications of changes in turbulent characteristics, the vertical behavior of the momentum amplification factor, γ, used to account for turbulence effects in integral models, changes considerably in the presence of a gas phase. In the thermal case, γ equilibrates to a reasonably constant value. In contrast, γ is initially smaller in the gas dominated plume, but continues to grow at all observed downstream locations.

The present model can be extended to study turbulent dynamics in more realistic representations of large-scale deep water releases. Using the same approach for the gas phase, it is possible to explicitly account for the presence of oil by considering the evolution of the nearly immiscible mixture of two liquid phases. Separating oil and thermal buoyancy contributions permits detailed evaluation of the effects of stratification on the multiphase system, including the role of turbulent mixing on the location and formation of lateral oil/gas intrusion layers. Additionally, by considering non-uniform slip velocities, or distributions of dispersed gas phases with different slip velocities, one may study bubble interaction and more complex, environmentally dependent biogeochemical processes including the investigation of dispersant effects.

Acknowledgments

This research is supported by a grant from BP/The Gulf of Mexico Research Initiative. Additional computer resources have also been provided by City University of New York High Performance Computing Center under NSF Grants CNS-0855217, CNS-0958379 and ACI-1126113.

References

Alendal, G., Drange, H., 2001. Two-phase, near-field modeling of purposefully released CO_2 in the ocean. J. Geophys. Res. 106, 1085–1096.
Asaeda, T., Imberger, J., 1993. Structure of bubble plumes in linearly stratified environments. J. Fluid Mech. 249, 35–57.
Batchelor, G.K., 1954. Heat convection and buoyancy effects in fluids. Q. J. R. Meteorol. Soc. 80, 339–358.
Boyd, J.P., 1998. Two comments on filtering (artificial viscosity) for Chebyshev and Legendre spectral and spectral element methods: preserving boundary conditions and interpretation of the filter as a diffusion. J. Comput. Phys. 143 (1), 283–288.
Brandvik, P.J., Johansen, Ø., Leirvik, F., Farooq, U., Daling, P.S., 2013. Droplet breakup in subsurface oil releases – part 1: Experimental study of droplet breakup and effectiveness of dispersant injection. Mar. Pollut. Bull. 73 (1), 319–326.
Buscaglia, G.C., Bombardelli, F.A., Garca, M.H., 2002. Numerical modeling of large-scale bubble plumes accounting for mass transfer effects. Int. J. Multiphase Flow 28, 1763–1785.
Camilli, R., Reddy, C.M., Yoerger, D.R., Van Mooy, B.A.S., Jakuba, M.V., Kinsey, J.C., McIntyre, C.P., Sylva, S.P., Maloney, J.V., 2010. Tracking hydrocarbon plume transport and biodegradation at Deepwater Horizon. Science 330 (6001), 201–204.
Cardoso, S.S.S., McHugh, S.T., 2009. Turbulent plumes with heterogeneous chemical reaction on the surface of small buoyant droplets. J. Fluid Mech. 642, 49–77.
Chen, C., Rodi, W., 1980. Turbulent Buoyant Jets: A Review of Experimental Data. Pergamon Press.
Clift, R., Grace, K.R., Weber, M.E., 1978. Bubbles, Drops and Particles. Academic Press.
Crespo-Medina, M., Meile, C., Hunter, K., Diercks, A.-R., Asper, V., Orphan, V., Tavormina, P., Nigro, L., Battles, J., Chanton, J., Shiller, A., Joung, D.-J., Amon, R., Bracco, A., Montoya, J., Villareal, T., Wood, A., Joue, A., 2014. The rise and fall of methanotrophy following a deepwater oil-well blowout. Nat. Geosci. 7, 423–427.
Deen, N.G., Solberg, T., Hjertager, B.H., 2001. Large eddy simulation of the gas-liquid flow in a square cross-sectioned bubble column. Chem. Eng. Sci. 56 (21–22), 6341–6349.
Dehaan, C., Sturges, W., 2005. Deep cyclonic circulation in the Gulf of Mexico. J. Phys. Oceanogr. 35, 1801–1812.

Deville, M.O., Fischer, P.F., Mund, E.H., 2002. High-Order Methods for Incompressible Fluid Flow. Cambridge University Press.
Dhotre, M.T., Deen, N.G., Niceno, B., Khan, Z., Joshi, J.B., 2013. Large eddy simulation for dispersed bubbly flows: a review. Int. J. Chem. Eng. 2013, 1–22.
Dhotre, M.T., Niceno, B., Smith, B.L., Simiano, M., 2009. Large-eddy simulation (LES) of the large scale bubble plume. Chem. Eng. Sci. 64, 2692–2704.
Ditmars, J.D., Cederwall, K., 1974. Analysis of air-bubble plumes. In: Coastal Engng. Conf., pp. 2209–2226. Chapter 128.
Drew, D.A., 1983. Mathematical modelling of two-phase flow. Annu. Rev. Fluid Mech. 15, 261–291.
Esmaeeli, A., Tryggvason, G., 1998. Direct numerical simulation of bubbly flows: Part 1. Low Reynolds number arrays. J. Fluid Mech. 377, 313–345.
Esmaeeli, A., Tryggvason, G., 1999. Direct numerical simulation of bubbly flows: Part 2. Moderate Reynolds number arrays. J. Fluid Mech. 385, 325–358.
Fischer, P. F., Lottes, J. W., Kerkemeier, S. G., 2008. Nek5000 web page. http://nek5000.mcs.anl.gov.
Fischer, P.F., Mullen, J.S., 2001. Filter-based stabilization of spectral element methods. Comptes rendus de lAcade mie des sciences Paris – Série I – Analyse numérique 332, 265–270.
Fox, R., 2012. Large-eddy simulation tools for multiphase flows. Annu. Rev. Fluid Mech. 44, 47–76.
George, W.K., Alpert, R.L., Tamanini, F., 1977. Turbulence measurements in an axisymmetric buoyant plume. Int. J. Heat Mass Transfer 20, 1145–1154.
Helfrich, K.R., 1994. Thermals with background rotation and stratification. J. Fluid Mech. 259, 265–280.
Johansen, Ø., Brandvik, P.J., Farooq, U., 2013. Droplet breakup in subsea oil releases – part 2: Predictions of droplet size distributions with and without injection of chemical dispersants. Mar. Pollut. Bull. 73 (1), 327–335.
Julien, K., Leff, S., McWilliams, J., Werne, J., 1999. Plumes in rotating convection. Part 1. ensemble statistics and dynamical balances. J. Fluid Mech. 391, 151–187.
Karamanos, G.-S., Karniadakis, G.E., 2000. A spectral vanishing viscosity method for large-eddy simulations. J. Comput. Phys. 163 (1), 22–50.
Koal, K., Stiller, J., Blackburn, H., 2012. Adapting the spectral vanishing viscosity method for large-eddy simulations in cylindrical configurations. J. Comput. Phys. 231 (8), 3389–3405.
Kuwagi, K., Ozoe, H., 1999. Three-dimensional oscillation of bubbly flow in a vertical cylinder. Int. J. Multiphase Flow 25 (1), 175–182.
Lemckert, C., Imberger, J., 1993. Energetic bubble plumes in arbitrary stratification. J. Hydraul. Eng. 119, 680–703.
Lima Neto, I.E., 2012. Modelling the liquid volume flux in bubbly jets using a simple integral approach. J. Hydraul. Eng. 138, 210–215.
Lima Neto, I.E., Zhu, D.Z., Rajaratnam, N., 2008a. Air injection in water with different nozzles. J. Environ. Eng. 134, 283–294.
Lima Neto, I.E., Zhu, D.Z., Rajaratnam, N., 2008b. Bubbly jets in stagnant water. Int. J. Multiphase Flow 34, 1130–1141.
List, E.J., Imberger, J., 1973. Turbulent entrainment in buoyant jets and plumes. J. Hydraul. Div. 99, 1461–1474.
McDougall, T.J., 1978. Bubble plumes in stratified environments. J. Fluid Mech. 85, 655–672.
McNutt, M., Camilli, R., Guthrie, G., Hsieh, P., Labson, V., Lehr, B., Maclay, D., Ratzel, A., Sogge, M., 2011. Assessment of Flow Rate Estimates for the Deepwater Horizon / Macondo Well Oil Spill. Technical Report. Flow Rate Technical Group report to the National Incident Command, Interagency Solutions Group.
Milgram, J.H., 1983. Mean flow in round bubble plumes. J. Fluid Mech. 133, 345–376.
Morton, B.R., Taylor, G., Turner, J.S., 1956. Turbulent gravitational convection from maintained and instantaneous sources. Proc. R. Soc. Lond. A 24, 1–23.
Niceno, B., Dhotre, M.T., Deen, N.G., 2008. One-equation sub-grid scale (sgs) modelling for euler-euler large eddy simulation (eeles) of dispersed bubbly flow. Chem. Eng. Sci. 63 (15), 3923–3931.
Özgökmen, T.M., Iliescu, T., Fischer, P.F., 2009a. Large eddy simulation of stratified mixing in a three-dimensional lock-exchange system. Ocean Modell. 26 (3–4), 134–155.
Özgökmen, T.M., Iliescu, T., Fischer, P.F., 2009b. Reynolds number dependence of mixing in a lock-exchange system from direct numerical and large eddy simulations. Ocean Modell. 30 (2-3), 190–206.
Roos, F.W., Willmarth, W.W., 1971. Some experimental results on sphere and disk drag. AIAA J. 9, 285–290.
Sato, T., Sato, K., 2002. Numerical prediction of the dilution process and its biological impacts in CO_2 ocean sequestration. J. Mar. Sci. Technol. 6, 169–180.
Sato, Y., Sadatomi, M., Sekoguchi, K., 1981. Momentum and heat transfer in two phase bubble flow, part 1 – theory. Int. J. Multiphase Flow 7, 167–177.
Schmidt, W., 1941. Turbulent propagation of a stream of heated air. Z. Angew. Math. Mech. 21, 265–351.
Schwarz, M.P., Turner, W.J., 1988. Applicability of the standard k-ϵ turbulence model to gas-stirred baths. Appl. Math. Model. 12, 273–279.
Shabbir, A., George, W.K., 1994. Experiments on a round turbulent buoyant plume. J. Fluid Mech. 275, 1–32.
Simiano, M., 2005. Experimental Investigation of Large-Scale Three Dimensional Bubble Plume Dynamics. Swiss Federal Institute of Technology Zurich (Ph.D. thesis).
Simonin, O., Viollet, P.L., 1990. Modeling of turbulent two-phase jets loaded with discrete particles. In: Phase-interface Phenomena in Multiphase Flows. Hemisphere Publishing Corp., pp. 259–269.
Socolofsky, S.A., Adams, E.E., 2003. Liquid volume fluxes in stratified multiphase plumes. J. Hydraul. Eng. 129, 905–914.
Socolofsky, S.A., Adams, E.E., 2005. Role of slip velocity in the behavior of stratified multiphase plumes. J. Hydraul. Eng. 131, 273–282.
Socolofsky, S.A., Adams, E.E., Sherwood, C.R., 2011. Formation dynamics of subsurface hydrocarbon intrusions following the Deepwater Horizon blowout. Geophys. Res. Lett. 38. doi:10.1029/ 2011GL047174.
Socolofsky, S.A., Crounse, B.C., Adams, E.E., 2002. Multiphase plumes in uniform, stratified and flowing environments. In: Cheng, A., Wang, K.-H., Teng, M.H., Liu, C. (Eds.), Environmental Fluid Mechanics Theories and Applications. ASCE, pp. 85–125.
Sokolichin, A., Eigenberger, G., Lapin, A., 2004. Simulation of buoyancy driven bubbly flow: established simplifications and open questions. AIChE J. 50(1), 24–45.
Tennekes, H., Lumley, J., 1972. A First Course in Turbulence. MIT Press.
Tomiyama, A., 1998. Struggle with computational bubble dynamics. In: Proceedings of the Third International Conference on Multiphase Flow, Lyon, France, pp. 11–18.
Turner, J., 1973. Buoyancy Effects in Fluids. Cambridge Monographs on Mechanics. Cambridge University Press.
Turner, J.S., 1969. Buoyant plumes and thermals. Annu. Rev. Fluid Mech. 1 (1), 29–44.
Yapa, P., Dissanayake, A., 2012. Discussion on a model to simulate the transport and fate of gas and hydrates released in deepwater. J. Hydraul. Res. 50, 646–649.
Zheng, L., Yapa, P., 2003. A model for simulating deepwater oil and gas blowouts. 1: Theory and model formulation. J. Hydraul. Res. 41, 339–351.